

March 2008

# Unusually low thermal conductivity of gallium nitride nanowires

Csaba Guthy
*University of Pennsylvania*

Chang-Yong Nam
*University of Pennsylvania*

John E. Fischer
*University of Pennsylvania*, fischer@seas.upenn.edu

# Unusually low thermal conductivity of gallium nitride nanowires

**Abstract**

We report measurements of thermal conductivity $\kappa$ on individual gallium nitride nanowires (GaN NWs) with diameters ranging from 97 to 181 nm grown by thermal chemical vapor deposition. We observed unexpectedly small kappa values, in the range of 13–19 W/m K at 300 K, with very weak diameter dependence. We also observe unusual power law $\kappa \sim T^n$ behavior with $n$=1.8 at low temperature. Electron-energy-loss-spectroscopy measurements indicate Si and O concentrations in the ranges of 0.1–1 and 0.01–0.1 at. %, respectively. Based on extensive numerical calculations, we conclude that both the unexpectedly low $\kappa$ and the $T^{1.8}$ dependence are caused by unusually large mass-difference scattering, primarily from Si impurities. Our analysis also suggests that mass-difference scattering rates are significantly enhanced by the reduced phonon group velocity in nanoscale systems. Planar defects running the length of the NW, previously characterized in detail, may also play a role in limiting the phonon mean free path.

# Unusually low thermal conductivity of gallium nitride nanowires

Csaba Guthy, Chang-Yong Nam, and John E. Fischer[a)]
*Department of Materials Science and Engineering, University of Pennsylvania, Philadelphia, Pennsylvania 19104, USA*

(Received 30 October 2007; accepted 8 January 2008; published online 28 March 2008)

We report measurements of thermal conductivity $\kappa$ on individual gallium nitride nanowires (GaN NWs) with diameters ranging from 97 to 181 nm grown by thermal chemical vapor deposition. We observed unexpectedly small $\kappa$ values, in the range of 13–19 W/m K at 300 K, with very weak diameter dependence. We also observe unusual power law $\kappa \sim T^n$ behavior with $n=1.8$ at low temperature. Electron-energy-loss-spectroscopy measurements indicate Si and O concentrations in the ranges of 0.1–1 and 0.01–0.1 at. %, respectively. Based on extensive numerical calculations, we conclude that both the unexpectedly low $\kappa$ and the $T^{1.8}$ dependence are caused by unusually large mass-difference scattering, primarily from Si impurities. Our analysis also suggests that mass-difference scattering rates are significantly enhanced by the reduced phonon group velocity in nanoscale systems. Planar defects running the length of the NW, previously characterized in detail, may also play a role in limiting the phonon mean free path. © *2008 American Institute of Physics*. [DOI: 10.1063/1.2894907]

## I. INTRODUCTION

Recently, the thermal properties of semiconductor nanowires (NWs) have become the subject of significant attention both for basic science and practical applications. Numerous theoretical calculations[1–3] predicted a significant decrease of the phonon thermal conductivity $\kappa$ of inorganic semiconductor NWs compared to the bulk value due to modification of phonon dispersion relation and increased boundary scattering at submicron length scales. A significant reduction is likely to create problems in thermal management of high speed and high power nanodevices. Conversely, low $\kappa$ could be advantageous for nanoscale solid-state energy conversion devices.[4]

Despite this interest,[1–3,5–8] experimental investigations are few in number. Shi *et al.*[9] developed a microdevice which uses two adjacent $SiN_x$ membranes suspended with long beams to measure $\kappa$ of individual freestanding NWs and nanotubes. Li *et al.*[10] studied diameter- and $T$-dependent $\kappa$ of Si NWs. While their results were in general agreement with predictions,[2] they observed a gradual transition from $T^3$ to linear $T$ dependence at low $T$ as Si NW diameter decreased from 110 to 22 nm. Since $\kappa(T)$ follows the $T$-dependent heat capacity for phonon transport, this implies one-dimensional phonon transport at 22 nm, much larger than expected.[11] Mingo[3] calculated $\kappa$ of Si NWs from complete phonon dispersions and obtained good overall agreement with Si NW data.[10] However, no discussion of low temperature $\kappa(T)$ and deviation from $T^3$ dependence was given.

Similar measurements were performed on several other NWs.[12–15] The high bulk $\kappa$ of GaN (Refs. 16 and 17) is one of the advantages of this wide band gap semiconductor material for high frequency, high power, and high temperature electronic and optoelectronic applications.[18–20] Despite the promise of GaN NWs for optoelectronic applications,[21–23] to our knowledge, there has been no experimental data reported to date on GaN NW $\kappa$. In contrast to the few nanometer thick amorphous surface oxide of Si NWs,[11] GaN NWs exhibit smooth well-developed facets with only a few monolayers of surface oxide.[24] The comparison of experimental $\kappa$ data on Si and GaN NWs, in principle, opens the opportunity to investigate the effects of the boundary scattering on thermal transport in these confined structures.

The rest of this paper is organized as follows. In Sec. II, we summarize the important characteristics of our GaN NWs based on our previous works[24,25] and describe the experimental "suspended island" technique and sample transfer method. Section III provides theoretical background upon which we draw to analyze and interpret our data. In Sec. IV, we present our results and discussion. Section V summarizes our findings and conclusions.

## II. EXPERIMENTAL DETAILS

Our GaN NWs were grown by thermal chemical vapor deposition (CVD) method[26] and were extensively characterized previously by Tham *et al.*[24,25] This analysis showed that these NWs preferentially grew in the [120] direction (perpendicular to the c axis) and had smooth surfaces along the growth axis and typically exhibited triangular (isosceles) cross sections. Most importantly, transmission electron microscopy (TEM) analysis[24] showed that the NWs contained numerous stacking faults (SFs) running along the entire NW length parallel to one of the facets (the (001) planes). Due to the presence of these extended defects, the low temperature phonon mean path (MFP) due to boundary scattering will be shorter than expected from the sample diameter and will be determined by the average interstacking fault separation.

To measure $\kappa$ of NWs, we developed our version of the technique, described in detail in Ref. 9. In short, in this suspended island method, one uses a microfabricated device with two adjacent low-stress silicon nitride ($SiN_x$) membrane islands, each suspended on five long $SiN_x$ beams (see Fig. 1).

[a)]Electronic mail: fischer@seas.upenn.edu.

 

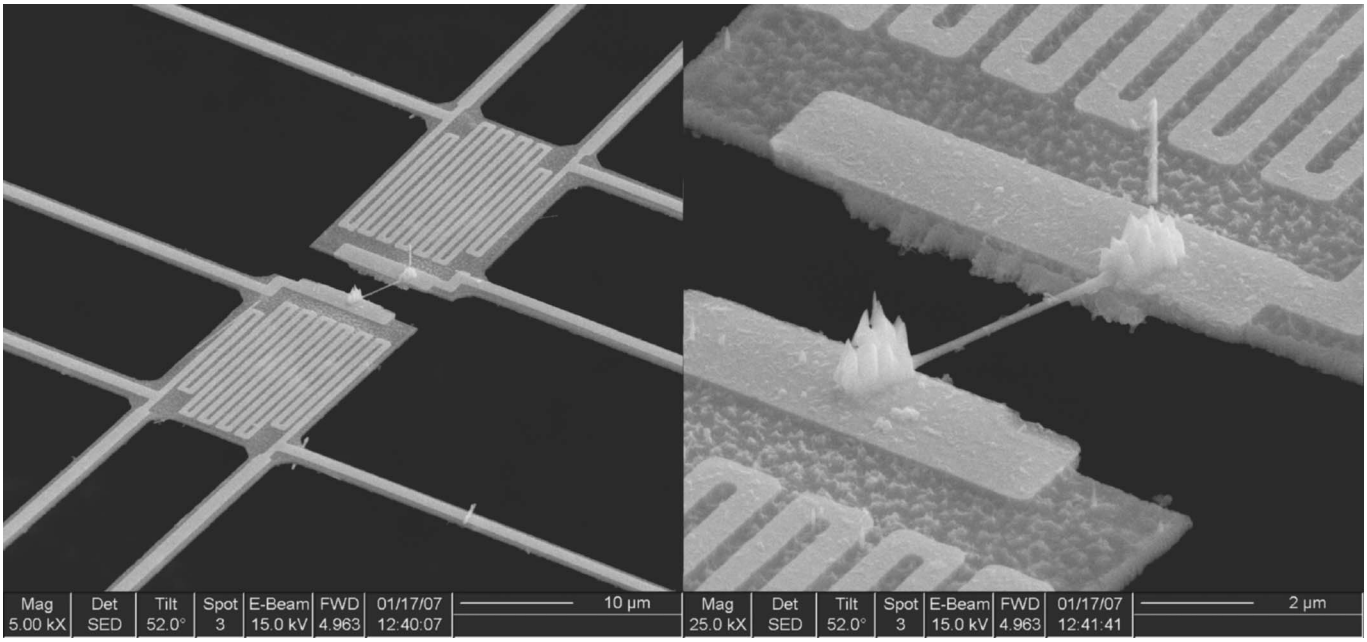


FIG. 1. SEM images of the suspended device showing the islands ($15\times25$ $\mu m^2$), suspending beams (500 nm$\times3$ $\mu$m$\times250$ $\mu$m), serpentine GRTs (30 nm thick) with connecting leads, and GaN NW bridging the islands. A dc current $I$ is applied to the heating GRTs. The generated Joule heat in the GRT and the two Au leads supplying the current raises the temperature of the heating island to $T_h$. The sample bridging the two islands conducts an amount of heat $Q_2$ from the heating island to the sensing one raising the temperature of the latter to $T_s$. $Q_2$ is further conducted to the environment at $T_0$ through the five beams suspending the sensing island. These five beams serve as a measure of the heat current $Q_2$ through the sample.

Gold resistance thermometers (GRTs) patterned on each island allow four-probe resistance measurements. Two Au electrodes at the tip of islands provide electrical contact to the sample bridging the islands and allow thermopower measurements. The suspended devices were fabricated using a combination of a two-step e-beam lithography and $SF_6$ reactive ion etching.

The two suspended islands with the GRTs on top allow one to establish a temperature gradient across the bridging NW sample by driving a large dc heating current $I$ through one of the GRTs (heating GRT). The temperature rises $\Delta T_h$ and $\Delta T_s$ of the heating and sensing islands, respectively, are determined from the changes of four-probe ac resistance measured using two SR830 digital lock-in amplifiers. In the case of the heating island, the large dc current has to be combined with a much smaller ac measuring current, which is accomplished using a summation amplifier and voltage-to-current converter. The heat current $Q_2$ conducted through the NW sample will be further conducted through the beams supporting the sensing islands, hence,

$$Q_2 = G_b(T_s - T_0) = G_s(T_h - T_s), \tag{2.1}$$

where $G_s$ and $G_b$ are the thermal conductions of the sample and beams, and $Q_h$ and $Q_L$ are the Joule heats generated by the dc current in the thermometer and two supplying leads, respectively. The Joule heats can be obtained from the known dc current $I$ and the measured dc resistances of heating GRT, $R_h$, and supplying leads, $R_L$ (from two- and four-probe dc resistances). Although the thermal conductance of the beams $G_b$ can be calculated from $\kappa$ of $SiN_x$ and the dimensions of the beams, $G_b$ can be obtained more accurately from measurement according to[9]

$$G_b = \frac{Q_h + Q_L}{\Delta T_h + \Delta T_s}. \tag{2.2}$$

Measurements were performed in a closed-cycle cold finger cryostat ($<10^{-6}$ Torr) in the temperature range of 22–320 K with fluctuations maintained below 20 mK. Measurement errors due to radiation loss were minimized by keeping $\Delta T$ across the sample in the range of 3–5 K and utilizing a radiation shield. To verify the validity of our measurements, we performed several tests. The resistance of GRTs showed linear temperature response in the 22–320 K range. The temperature rises $\Delta T_h$ and $\Delta T_s$ of both the heating and sensing islands showed linear response with applied dc power ($I^2$) at various temperatures. The coupling of the dc and ac currents affects the response of the heating thermometer at intermediate frequencies.[9] To avoid these frequencies, we measured the resistance change of the heating GRT in response to a constant dc current as a function of measuring signal frequency at 22, 56, 96, 195, and 298 K. Based on these considerations, we chose our working frequency of 2274 Hz in the whole temperature range and for all samples since all of our devices have the same dimensions and, hence, thermal time constant $\tau$.

The nanostructures can be transferred from the substrate to the suspended device just by putting the substrate in close proximity of the suspended structure facing it. From our experience, a large number of nanostructures will be transferred this way though in a random fashion. This method requires numerous attempts (on the order of 100) to successfully place a NW on the suspended structure such that it bridges the two islands. After each attempt, the gap between the islands was examined under an optical microscope for the presence of a NW. Once a promising transfer is detected,

the structure is examined in scanning EM (SEM) to confirm the presence of the NW. Despite its tediousness, we chose this "dry transfer" method because it provides a clean transfer of NWs without any solvent residue.

To improve the thermal and electrical contact between the NW and the islands, the structure is transferred into a dual beam focused ion beam (FIB) system (FEI Strata DB235). The contacts are improved by focused electron beam (FEB) Pt deposition (see Fig. 1). Even though FIB deposition results in a significantly better quality (lower resistivity) Pt, we decided to use FEB deposition. The reason behind this is that from our experience,[27] FIB exposure results in significant damage (amorphization) of the NWs. The wires that would interfere with the measurement are cut away using FIB.

## III. CALLAWAY MODEL AND PHONON SCATTERING PROCESSES

We analyzed our results within the framework of the (pretty standard) Callaway model[28,29] of heat conduction. The thermal conductivity $\kappa$ is given as

$$\kappa(T) = \left(\frac{k_B}{\hbar}\right)^3 \frac{k_B}{2\pi^2 v_G} T^3 \int_0^{\theta_D/T} \frac{\tau x^4 e^x}{(e^x - 1)^2} dx, \tag{3.1}$$

where $\theta_D$ is the Debye temperature, $k_B$ is the Boltzmann constant, $v_G$ is the phonon group velocity, $x=\hbar\omega/k_BT$, $\omega$ is the phonon frequency, and $\tau_C$ is the combined phonon relaxation time. In the Callaway expression, the cutoff frequency is the Debye frequency $\omega_{\max}$, which is obtained from the condition that the total number of modes is $3N$,

$$\omega_{\max} = \sqrt[3]{\frac{6\pi^2}{V_0}} v_G, \tag{3.2}$$

where $V_0$ is the volume of a unit cell and $\theta_D=\hbar\omega_{\max}/k_B$ is the Debye temperature. The two important parameters influencing $\kappa$ are the phonon group velocity $v_G$ and the combined relaxation time $\tau_C$. We discuss next what goes into $\tau_C$.

We consider the following major phonon scattering processes which limit $\kappa$ of a solid: three-phonon umklapp, boundary, mass-difference (impurity and isotope), and phonon-electron scatterings. Normal processes are only important for isotopically pure crystals and are, therefore, neglected in our analysis (the natural Ga isotope composition is 60:40 $^{69}$Ga:$^{71}$Ga). According to Matheissen's rule, the inverse combined phonon relaxation time (or combined phonon scattering rate) $\tau_C^{-1}$ is the sum of the individual inverse relaxation times,

$$\frac{1}{\tau_C} = \frac{1}{\tau_U} + \frac{1}{\tau_B} + \frac{1}{\tau_M} + \frac{1}{\tau_{\text{ph-}e}}. \tag{3.3}$$

The scattering rate for umklapp processes can be written as[2]

$$\tau_U^{-1} = C_2 \omega^2 T e^{-C_3/T}, \tag{3.4}$$

where constants $C_2$ and $C_3$ are usually determined from the best fit of bulk experimental data.

When at low temperatures, the MFP becomes comparable to the NW diameter, $\kappa$ becomes a function of sample dimensions. Boundary scattering is also responsible for the $T^3$ low temperature dependence of three-dimensional (3D) bulk $\kappa$. The scattering rate can be written as

$$\tau_B^{-1} = \frac{v_G}{L_C}, \tag{3.5}$$

where $L_C$ represents the effective MFP, or Casimir length, and is of the order of the cross-sectional dimensions. It takes into account the sample size, geometry, aspect ratio, specular/diffuse scattering at the surface, etc. For a circular cylinder with radius $R$, this length is equal to $L_C=2R=D$. However, partial specularity of phonon scattering can increase the effective MFP above the sample cross-sectional size and cause a deviation from the low temperature $T^3$ dependence.[30–32]

In a crystal containing a low concentration of atoms of different masses, phonons will be scattered by the mass difference. The scattering rate is given by the Rayleigh formula,[33]

$$\tau_M^{-1} = \frac{\Gamma V_0 \omega^4}{4\pi v_G^3}, \tag{3.6}$$

where $\Gamma$ measures the strength of the scattering,

$$\Gamma = \sum_i f_i \left(1 - \frac{M_i}{M}\right), \tag{3.7}$$

where $f_i$ is the fraction of sites occupied by atoms of mass $M_i$ and $M=\Sigma_i f_i M_i$ is the average mass.

Ziman calculated the phonon-electron scattering rate using the effective mass approximation and obtained[34]

$$\tau_{\text{ph-}e}^{-1} = \frac{E_1^2 m_{\text{eff}}^2 k_B T}{2\pi\hbar^4 \rho \cdot v_L} \left[ \frac{\hbar\omega}{k_B T} - \ln \frac{1 + \exp\left(\Psi + \frac{\hbar\omega}{2k_B T}\right)}{1 + \exp\left(\Psi - \frac{\hbar\omega}{2k_B T}\right)} \right], \tag{3.8}$$

where

$$\Psi = \frac{\hbar^2\omega^2}{8 m_{\text{eff}} v_L^2 k_B T} + \frac{m_{\text{eff}} v_L^2}{2k_B T} - \frac{E_F}{k_B T} \tag{3.9}$$

for the scattering of longitudinal phonons. $E_1$ is a constant specifying the strength of the phonon-electron interaction and is called the deformation potential, $E_F$ is the Fermi energy, $m_{\text{eff}}$ is the electron effective mass, $\rho$ is the density, and $v_L$ is the velocity of longitudinal phonons.

Assuming donors only, the Fermi energy is given by[35]

$$E_F = E_g - E_d + k_B T \ln\left[ -\frac{1}{4} + \sqrt{\frac{1}{16} + \frac{N_D}{2N_C} \exp\left(\frac{E_d}{k_B T}\right)} \right], \tag{3.10}$$

where $E_d$ is the donor ionization energy, $E_g$ is the energy gap, $N_D$ is the donor concentration, and $N_C$ is the density of states near the conduction band edge and is given by[35]

$$N_C(T) = 2\left(\frac{2\pi m_{\text{eff}} k_B T}{\hbar^2}\right)^{1.5}. \tag{3.11}$$

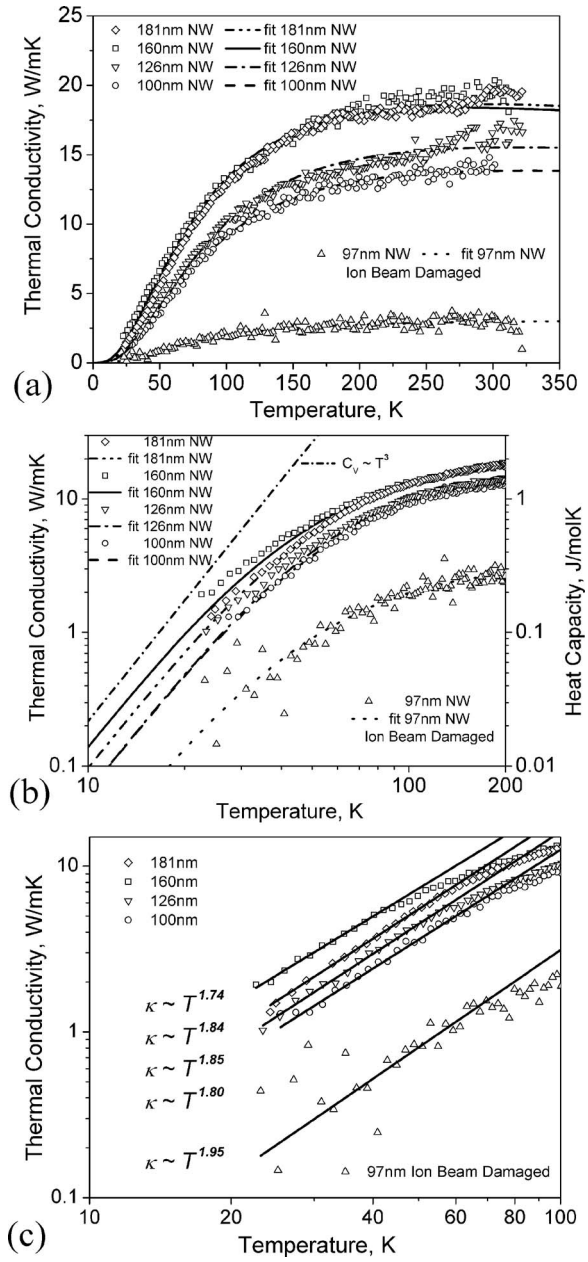


FIG. 2. (a) Temperature dependence of the experimental $\kappa$ of GaN NWs in the range of 24–320 K and the best fits using the Callaway approach. All samples with apparent triangular cross sections (160, 100, 126, and 181 nm) have very similar room $T$ $\kappa$ in the range of 13–19 W/m K. The much lower $\kappa$ of 97 nm sample is due to FIB damage. (c) All samples exhibit an unusual $T^{1.8}$ low temperature $\kappa$ dependence (note the log-log scale). The fits will be discussed later.

## IV. RESULTS AND DISCUSSION

Figure 2(a) shows $\kappa$ vs $T$ for five GaN NW samples with "diameters" ranging from 97 to 181 nm and length of $\sim 5$ $\mu$m. The smallest one exhibits a significantly lower $\kappa$ at all $T$ compared to the other four with $\kappa$(300 K) values in the range of 13–19 W/m K. The much lower $\kappa$ of the 97 nm sample can be attributed to unintentional FIB induced damage, as apparent from SEM and observed previously.[36] The 17 W/m K average is surprisingly low compared to reported bulk values of 130–220 W/m K.[16,17] To verify that $\kappa$ is not limited by the electron beam contacts, we measured several samples with different contact areas (different amounts of FEB deposited Pt) and different diameters (160, 100, and 181 nm) and found no systematic differences. If contact resistance was limiting the heat transport, we should observe a decreasing apparent $\kappa$ with increasing NW diameter. Therefore, we conclude that the thermal conduction in our suspended devices is not limited by the thermal contact resistance and the observed significant reduction of NW $\kappa$ is real.

Plotting the thermal conductivity in log-log scale [Fig. 2(c)] gives a low temperature slope of $\sim 1.8$ for all samples. One would expect $T^3$ dependence signaling 3D behavior for diameters in the range of 100–200 nm, while the 1.8 exponent is closer to two-dimensional behavior. This is fortuitous and has nothing to do with dimensional crossover, as we show in the following.

To calculate $\kappa$, we first need to determine the parameters $C_2$ and $C_3$ of the umklapp scattering rate [Eq. (3.4)]. We followed the approach of Ref. 3 and obtained these by fitting bulk experimental data[17] from which we obtained $C_2 = (2.47) \times 10^{-19}$ s/K and $C_3 = 230.7$ K. Also required are the mass density $\rho = 6150$ kg/m$^3$, molar mass $M = 83.73 \times 10^3$ kg/mol, and phonon group velocity $v_G = 5071$ m/s according to

$$v_G = \frac{3}{v_L^{-1} + v_{T1}^{-1} + v_{T2}^{-1}}, \tag{4.1}$$

where $v_L$, $v_{T1}$, and $v_{T2}$ are the longitudinal and two transverse phonon velocities. The latter are calculated from the values of 390, 145, and 105 GPa (Ref. 37) for the elastic constants $c_{11}$, $c_{12}$, and $c_{44}$, respectively,

$$v_L = \sqrt{\frac{c_{11}}{\rho}}, \tag{4.2}$$

$$v_{T1} = \sqrt{\frac{c_{44}}{\rho}}, \tag{4.3}$$

$$v_{T2} = \sqrt{\frac{c_{11} - c_{12}}{2\rho}}. \tag{4.4}$$

The Debye cutoff frequency is calculated from $v_G$ according to Eq. (3.2), where the atomic volume $V_0 = \sqrt{3}a^2c/4$ with $a = 3.189$ Å and $c = 5.185$ Å for wurtzite GaN.[37]

Two adjustable parameters were used to obtain the best fits: the Casimir length ($L_C$) and the mass-difference scattering parameter $\Gamma$. $\Gamma$ for bulk samples is well specified by the precisely controlled dopant concentrations. Here, the GaN NWs are unintentionally doped with O and Si during CVD growth. From electron-energy-loss spectroscopy (EELS) analysis, we estimate the concentrations of Si and O to be 0.1–1 and 0.01–0.1 at. %, respectively.[24] This high carrier concentration ($2.3 \times 10^{19}$ cm$^{-3}$) also necessitates accounting for phonon-electron scattering, which was calculated according to Eqs. (3.8) and (3.9) with a deformation potential of 10.1 eV (Ref. 38) and electron effective mass of $0.22m_e$.[39] The Fermi level $E_F$ was calculated according to Eqs. (3.10) and (3.11) with ionization energies $E_d$ of 30.8 and 32.4 meV for Si and O, respectively.[40] Because of the presence of SFs, the Casimir length $L_C$ will be limited by average interstacking fault separation rather than sample diameter. Details of

TABLE I. Casimir length $L_C$ and mass-difference factor $\Gamma$ obtained from the best fits of experimental GaN NW $\kappa$ data using the bulk phonon group velocity $v_G$ of 5071 m/s.

| "Diameter" (nm) | Length ($\mu$m) | Casimir length $L_C$ (nm) | Mass-difference scattering parameter $\Gamma$ |
|---|---|---|---|
| 160 | 5 | 89 | $1.60\times10^{-2}$ |
| 100 | 5 | 41 | $1.64\times10^{-2}$ |
| 97 | 5 | 12 | $10.34\times10^{-2}$ |
| 126 | 5 | 41 | $1.34\times10^{-2}$ |
| 181 | 5 | 62 | $1.26\times10^{-2}$ |

individual sample morphologies were not determined, thus, the rationale for including $L_C$ as a fit parameter.

As Figs. 2(a) and 2(b) illustrate, we were able to obtain very good fits to the experimental data. The parameters obtained from the best fit are summarized in Table I below. We can see from Table I that $L_C$ is a factor of 2-4 lower than the sample diameter, which we attribute to the presence of SFs. A somewhat surprising result was that the mass-variance factor $\Gamma$ obtained from the fits is significantly higher (almost two orders of magnitude) than the value of $2.16\times10^{-4}$ calculated based on Eqs. (3.6) and (3.7) for pure GaN. We attribute this to the high dopant concentration of Si and O.

To illustrate which scattering mechanism dominates the heat transport at various temperatures, we calculated the MFP due to each scattering mechanism as a function of phonon frequency $\omega$ at 5, 30, 80, and 300 K for the 181 nm sample [see Figs. 3(a)–3(d)], respectively. The differential thermal conductivity $\kappa_{\text{diff}}$ plotted as a function of $\omega$ shows which phonon frequencies dominate the heat transport at a given temperature. The total $\kappa$ is given by the area underneath the $\kappa_{\text{diff}}$ curve. Note the log-log scale. This analysis shows that the unusually high mass-difference scattering rates are responsible for the deviation from the $T^3$ low temperature $\kappa$ dependence.

At 5 K, the combined MFP of dominant phonons is determined exclusively by boundary scattering [see Fig. 3(a)] which is independent of $\omega$, as is the group velocity $v_G$. Thus, $\kappa$, which is the product of MFP, $v_G$, and the heat capacity $C_p$ will have $T^3$ dependence at low $T$ for NWs of this size. However, specular scattering of low frequency phonons may also result in deviation from $T^3$ dependence.[30–32]

At 30 K, the scattering rates are largely unchanged [see Fig. 3(b)] compared with those at 5 K with the exception of increased umklapp scattering. However, umklapp scattering rates are not high enough to limit the combined MFP. The main change comes from the shift to higher dominant phonon frequencies. Mass-difference scattering of the higher fre-

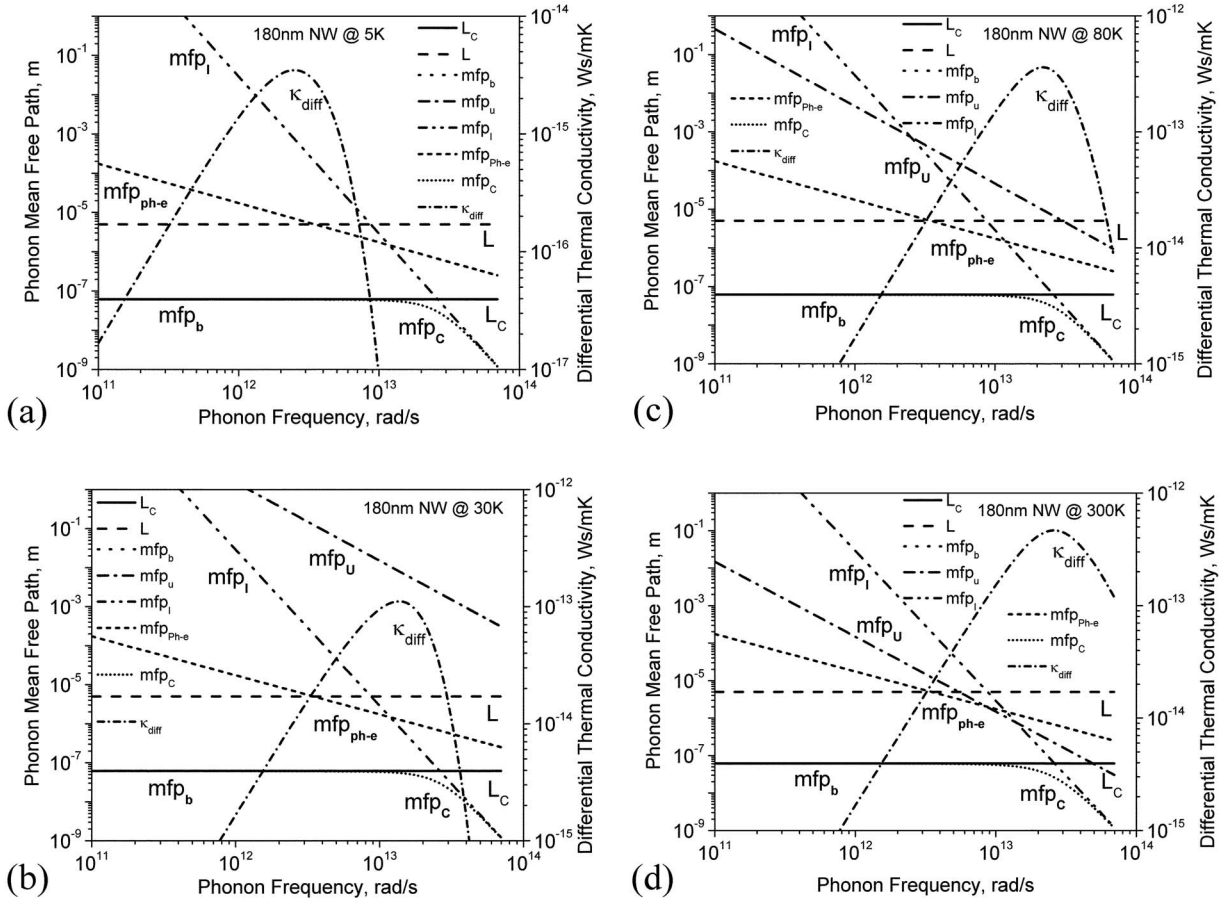


FIG. 3. Phonon mean free path (MFP) due to different scattering mechanisms as a function of phonon angular frequency for the 181 nm GaN NW sample at (a) 5, (b) 30, (c) 80, and (d) 300 K. The dotted, dash-dot, dash-dot-dot, and short dashed lines represent the MFP due to boundary, umklapp, mass-difference, and phonon-electron scatterings, respectively. The dotted line represents the combined MFP, while the short dash-dot designates the differential thermal conductivity.

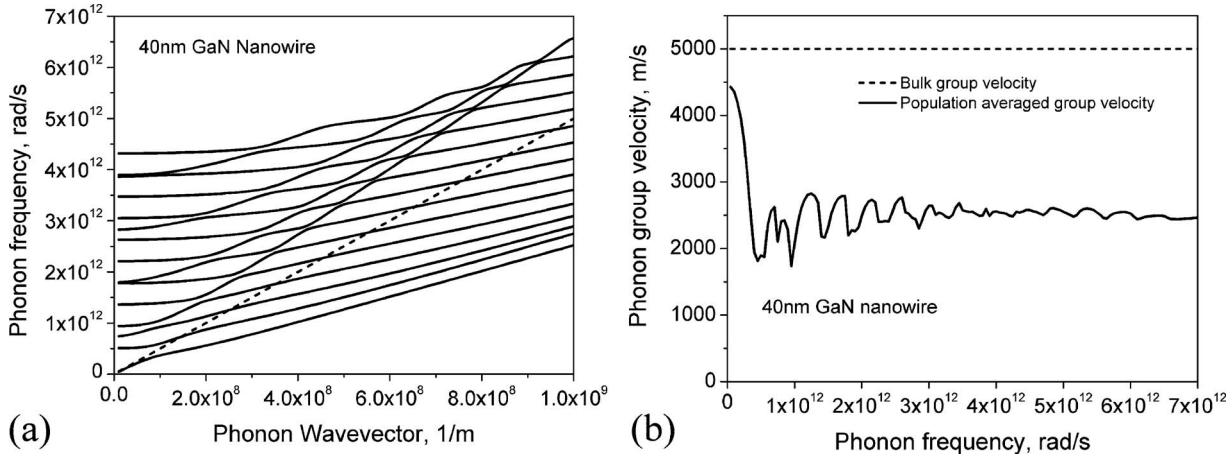


FIG. 4. (a) Acoustic phonon dispersion curves for the 15 lowest confined branches in a GaN nanowire with a diameter of 40 nm. (b) Population-averaged phonon group velocity as a function of phonon frequency. The group velocity converges to a reduced value of ~2500 m/s compared to the bulk value of ~5000 m/s.

quency phonons starts to limit $\kappa$, although only to a small extent. The combined MFP is largely limited by boundary scattering from SFs.

As temperature increases from 30 to 300 K, the phonons dominating the heat transport gradually shift to higher $\omega$ [see Figs. 3(c) and 3(d)]. The phonon MFP and, therefore, $\kappa$ become more and more limited by impurity rather than boundary scattering. This gradual shift is responsible for the deviation from $T^3$ dependence. The higher the defect/impurity concentration is, the lower the onset of this deviation is. Although the umklapp scattering rates are increasing as the temperature is raised, their magnitude does not reach that of impurity scattering even at 300 K. The strength of the phonon-electron scattering is not high enough to limit the combined MFP at any temperature.

As mentioned earlier, the fitted mass-variance factor $\Gamma$ was significantly higher than the value calculated for clean GaN. Assuming Si as the main impurity, the obtained $\Gamma$ corresponds to an unreasonably high concentration (~10 at. %) of Si impurities. A natural explanation for this contradiction lies in the inverse cubic dependence of mass-difference scattering rates on $v_G$ [see Eq. (3.6)]. Even a moderate reduction in $v_G$ will significantly enhance the mass-difference scattering rates. To estimate the reduction of $v_G$ in our GaN NWs, we followed the approach of Zou and Balandin to calculate phonon dispersion of the confined acoustic modes. Their results for a freestanding cylindrical Si quantum wire with diameter of 20 nm showed that $v_G$ was reduced ~ twofold from the bulk value.[2]

The results of our calculations are presented in Figs. 4(a) and 4(b). Figure 4(a) shows the acoustic phonon dispersion curves for the 15 lowest confined branches (solid lines) in a 40 nm diameter GaN NW. The dashed line designates the bulk (Debye) dispersion relation. Similar to the results in Ref. 2, we find that only the first branch has a linear dispersion for very small values of wave vector $q$, while all other branches have a lower cutoff frequency. The slope of all phonon branches is lower than those in the bulk resulting in reduced $v_G$. The population-averaged $v_G$ is shown in Fig. 4(b) as a function of phonon frequency. The average $v_G$ is reduced by half compared to the bulk value [dashed line in Fig. 4(b)] starting at a $\omega \sim 5 \times 10^{11}$ rad/s. Figures 3(b)–3(d) show that in the 25–320 K experimental temperature range, the frequency of dominant phonons lies in this reduced $v_G$ range. Thus, for a freestanding 40 nm diameter GaN NW, a constant group velocity of 2500 m/s can be used.

The diameter of investigated GaN NWs ranges from 97 to 181 nm. Therefore, we expect a smaller $v_G$ reduction than calculated for a 40 nm NW. It is also likely that the onset of $v_G$ reduction starts at higher $\omega$. It should also be noted that strictly speaking, the results are only valid for circular NWs; thus, the obtained reduction is not exact.

We take $v_G$ as an adjustable parameter and assume that the impurity concentrations are the same in all samples and are equal to the upper limit of experimentally determined impurity concentrations (1 at. % Si, 0.1 at. % O, and 0.1 at. % of $V_{Ga}$ from EELS analysis). The obtained fits are very similar to those in Figs. 2(a) and 2(b). The best fit parameters are summarized in Table II. Recall that the 97 nm sample sustained substantial Ga ion beam damage which is known to increase the nitrogen vacancy ($V_N$) concentration.[41] Due to the low formation energy of Ga vacancies ($V_{Ga}$) under Ga-rich conditions[42] and high binding energy[43] of the $V_{Ga}$-$V_N$ complex, we expect higher $V_{Ga}$ concentration as well. For this sample, we therefore used a

TABLE II. Parameters of the best fit (Casimir limit $L_C$ and reduced $v_G$) assuming the upper limit (1 at. % Si and 0.1 at. % O) of EELS data for the impurity concentrations in all samples, except the ion beam damaged 97 nm sample (4 at. % $V_{Ga}$).

| "Diameter" (nm) | Length ($\mu$m) | Casimir limit $L_C$ (nm) | Reduced group velocity $v_G$ (m/s) |
|---|---|---|---|
| 160 | 5 | 35 | 3800 |
| 100 | 5 | 18 | 3700 |
| 97 | 5 | 5 | 3800 |
| 126 | 5 | 21 | 3800 |
| 181 | 5 | 33 | 3800 |

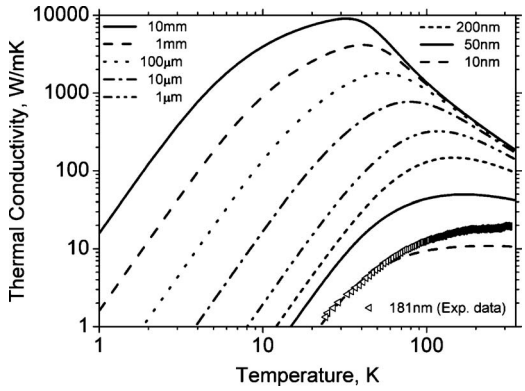


FIG. 5. Temperature dependence of thermal conductivity of "impurity-free" GaN for samples with diameters $d$ in the range of 10–10 nm. The calculations are performed with the assumption that the sample length $L \gg d$. For comparison, the experimentally measured thermal conductivity of the GaN sample with a diameter of 181 nm (triangles) is shown as well. The significant decrease of $\kappa$ compared to the theoretical curve for a 200 nm wire is due to the high impurity concentration in the nanowire.

higher $V_{Ga}$ concentration (4 at. %). It can be seen from the results that $v_G$ had to be reduced to ~3700–3800 m/s. This reduction in $v_G$ increases the mass-difference scattering rates such that a lower impurity concentration is adequate to obtain a good fit. The reduced $v_G$ also reduces the boundary scattering rates, thus, requiring shorter $L_C$, indicating a higher density of SFs compared to those in Table I.

The presence of SFs complicates the analysis for several reasons. We have observed[24] that the SFs always run parallel to each other and to one of the NW facets and in this way, they dissect the NW into several "slabs." In addition, the interstacking fault separation is not constant and SFs tend to be more closely spaced in the apex of the triangular cross section. Because of this, these NWs consist of several regions with different "local" $\kappa$: the regions in the apex have small cross sections and, therefore, will have a low $\kappa$ (due to size effect); there is a thicker "core" region (no SFs and larger width) which is expected to dominate the thermal transport.

All the above factors are responsible for the discrepancies between the experimental and calculated fitting parameters. Nevertheless, these discrepancies are small and do not change the basic physical picture of the reduced heat transfer in our thermal CVD grown GaN NWs: the low temperature $\kappa$ is limited by boundary scattering from the NW surface and SFs; the room temperature $\kappa$ is mainly limited by the unusually large mass-difference scattering due to high impurity concentration as well as enhancement of the mass-difference scattering rates as a result of decreased phonon group velocity.

The experimental $\kappa$ values are surprisingly low, due to high impurity concentration which is unavoidable in our growth method. It is possible to grow GaN NWs with much lower impurity levels using molecular beam epitaxy in ultrahigh vacuum.[44,45] In this section, we investigate $\kappa$ of hypothetical "pure" GaN (mass-difference scattering from the natural isotope concentration only) as a function of diameter. GaN with Si and other impurity concentration of $<10^{16}$ cm$^{-3}$ would be close to this idealized situation. Figure 5 shows $\kappa$ vs $T$ for pure GaN for diameters from 10 to 10 nm.

As expected, $\kappa$ at a given low $T$ is proportional to diameter, consistent with the MFP being limited by boundary scattering. In contrast, the size dependence becomes negligible at high $T$, down to ~1 $\mu$m because the combined phonon MFP is limited by umklapp scattering. Below 1 $\mu$m, the phonon MFP due to boundaries becomes smaller than that due to umklapp. At these sizes, one also expects reduction of the phonon group velocity and, hence, increase of mass-difference scattering. This leads to a further reduction of $\kappa$. For a 50 nm GaN NW, $\kappa$ at 300 K is expected to decrease by a factor of ~5 (to 40 W/m K). For comparison, we also included the experimental $\kappa$ of the 181 nm GaN NW sample. It can be seen that this curve lies very close to that calculated for a 10 nm pure GaN NW. It is also lower by a factor of ~5 compared to the curve calculated for pure GaN with a diameter of 200 nm. We attribute this significant reduction to the high impurity levels. These results show that even for pure GaN, $\kappa$ is significantly reduced as the diameter of the wire approaches the sub-100 nm regime. This reduction would be present even if no phonon confinement occurred as the size is decreased, simply because the sample boundaries limit the phonon MFP. It should be noted that for samples with very smooth surface, the low $T$ phonon MFP might be longer than the sample diameter due to specular scattering of phonons. However, at higher temperatures, higher frequency phonons dominate the heat transport, and even a very small surface roughness will result in diffusive scattering. This result suggests that the promising electrical properties of semiconductor NWs, in general, might be overshadowed by the significant reduction of $\kappa$. Nevertheless, the situation might not be as hopeless as it seems. The size reduction also increases the surface-to-volume ratio, thus, allowing more efficient heat dissipation between NW and substrate. The reduced $\kappa$ also has its advantages, especially in thermoelectric devices. The very high resistance (on the order of gigohms) of FEB deposited Pt contacts prevented us from obtaining reliable thermopower data. To estimate the figure of merit $ZT$, we use the thermopower of bulk GaN (~120 $\mu$V/K) (Ref. 46) and the two-probe resistivity value of $\sim 1.4 \times 10^{-4}$ $\Omega$ m (Ref. 47) obtained for a 150 nm GaN NW contacted using e-beam lithography. We estimate the $ZT$ of our GaN NWs to be 0.0018.

## V. CONCLUSIONS

We report the first experimental investigation of thermal conductivity in individual freestanding GaN NWs. The diameters of the studied NW samples were in the range of 97–181 nm and they were grown by thermal CVD method. We observed an unexpectedly large $\kappa$ reduction as well as a strange $T^{1.8}$ low temperature dependence. In addition, we have found very weak correlation between room temperature $\kappa$ and NW diameters, indicating that the phonon scattering mechanism limiting the MFP is independent of the NW cross section. Our GaN NWs contain numerous SFs running their whole length parallel to one of the facets. TEM analysis also revealed high impurity levels of Si and O in the ranges of 0.1–1 and 0.01–0.1 at. %, respectively. Based on the comparison of our numerical calculations according to the Calla-

way model with our experimental data, we conclude that the unexpectedly large reduction of $\kappa$ as well as the strange $T^{1.8}$ temperature dependence are a result of the very high mass-difference scattering of phonons from Si and O impurities and Ga vacancies. The mass-difference scattering rates are likely to be enhanced due to the reduced phonon group velocity in these confined structures. SFs also play an important role in limiting the phonon MFP, especially at low temperatures. The large $\kappa$ reduction is advantageous for thermoelectric power generation. Although the estimated $ZT$ of 0.0018 for our GaN NWs is low compared to those of the current commercial thermoelectrics, further enhancements are expected if the NW properties are deliberately tailored to reduce $\kappa$ without degrading their thermoelectric properties.

## ACKNOWLEDGMENTS

We are grateful to Aaron Stein and James Misewich for valuable advice and assistance in the early phases of this work. Support was provided by the Department of Energy, No. DE-FG02-98ER45701.

[1] A. Balandin and K. L. Wang, Phys. Rev. B **58**, 1544 (1998).
[2] J. Zou and A. Balandin, J. Appl. Phys. **89**, 2932 (2001).
[3] N. Mingo, Phys. Rev. B **68**, 113308 (2003).
[4] L. D. Hicks and M. S. Dresselhaus, Phys. Rev. B **47**, 16631 (1993).
[5] Y. F. Chen, D. Y. Li, J. R. Lukes, and A. Majumdar, ASME Trans. J. Heat Transfer **127**, 1129 (2005).
[6] A. V. Zhukov, S. Yang, and J. Cao, JETP Lett. **81**, 190 (2005).
[7] W. X. Li, K. Q. Chen, W. H. Duan, W. Jian, and B. L. Gu, J. Phys. D **36**, 3027 (2003).
[8] T. Prosen and D. K. Campbell, Phys. Rev. Lett. **84**, 2857 (2000).
[9] L. Shi, D. Y. Li, C. H. Yu, W. Y. Jang, D. Kim, Z. Yao, P. Kim, and A. Majumdar, ASME Trans. J. Heat Transfer **125**, 881 (2003).
[10] D. Y. Li, Y. Y. Wu, P. Kim, L. Shi, P. D. Yang, and A. Majumdar, Appl. Phys. Lett. **83**, 2934 (2003).
[11] K. W. Adu, H. R. Gutierrez, U. J. Kim, G. U. Sumanasekera, and P. C. Eklund, Nano Lett. **5**, 409 (2005).
[12] J. H. Zhou, C. G. Jin, J. H. Seol, X. G. Li, and L. Shi, Appl. Phys. Lett. **87**, 133109 (2005).
[13] F. Zhou, J. Szczech, M. T. Pettes, A. L. Moore, S. Jin, and L. Shi, Nano Lett. **7**, 1649 (2007).
[14] D. Y. Li, Y. Wu, R. Fan, P. D. Yang, and A. Majumdar, Appl. Phys. Lett. **83**, 3186 (2003).
[15] L. Shi, Q. Hao, C. H. Yu, N. Mingo, X. Y. Kong, and Z. L. Wang, Appl. Phys. Lett. **84**, 2638 (2004).
[16] E. K. Sichel and J. I. Pankove, J. Phys. Chem. Solids **38**, 330 (1977).
[17] A. Jezowski, B. A. Danilchenko, M. Bockowski, I. Grzegory, S. Krukowski, T. Suski, and T. Paszkiewicz, Solid State Commun. **128**, 69 (2003).
[18] S. Nakamura, S. Pearton, and G. Fasol, *The Blue Laser Diode: The Complete Story* (Springer-Verlag, Berlin, 2000), pp. 7–9.
[19] S. J. Pearton and F. Ren, Adv. Mater. (Weinheim, Ger.) **12**, 1571 (2000).
[20] S. N. Mohammad, A. A. Salvador, and H. Morkoc, Proc. IEEE **83**, 1306 (1995).
[21] Y. Huang, X. F. Duan, Y. Cui, and C. M. Lieber, Nano Lett. **2**, 101 (2002).
[22] J. C. Johnson, H. J. Choi, K. P. Knutsen, R. D. Schaller, P. D. Yang, and R. J. Saykally, Nat. Mater. **1**, 106 (2002).
[23] S. Gradecak, F. Qian, Y. Li, H. G. Park, and C. M. Lieber, Appl. Phys. Lett. **87**, 173111 (2005).
[24] D. Tham, C. Y. Nam, and J. E. Fischer, Adv. Funct. Mater. **16**, 1197 (2006).
[25] D. Tham, C. Y. Nam, K. Byon, J. Kim, and J. E. Fischer, Appl. Phys. A: Mater. Sci. Process. **85**, 227 (2006).
[26] C. Y. Nam, D. Tham, and J. E. Fischer, Appl. Phys. Lett. **85**, 5676 (2004).
[27] C. Y. Nam, D. Tham, and J. E. Fischer, Nano Lett. **5**, 2029 (2005).
[28] J. Callaway, Phys. Rev. **113**, 1046 (1959).
[29] R. Berman, *Thermal Conduction in Solids* (Clarendon, Oxford, 1976).
[30] M. Asen-Palmer, K. Bartkowski, E. Gmelin, M. Cardona, A. P. Zhernov, A. V. Inyushkin, A. Taldenkov, V. I. Ozhogin, K. M. Itoh, and E. E. Haller, Phys. Rev. B **56**, 9431 (1997).
[31] S. B. Soffer, J. Appl. Phys. **38**, 1710 (1967).
[32] D. P. Singh and Y. P. Joshi, Phys. Rev. B **19**, 3133 (1979).
[33] J. E. Parrott and A. D. Stuckes, *Thermal Conductivity of Solids* (Pion, London, 1975), pp. 64–65.
[34] J. E. Parrott, Rev. Int. Hautes Temp. Refract. **16**, 393 (1979).
[35] S. M. Sze, *Physics of Semiconductor Devices*, 2nd ed. (Wiley-Interscience, New York, 1981).
[36] D. Tham, C. Y. Nam, and J. E. Fischer, Adv. Mater. (Weinheim, Ger.) **18**, 290 (2006).
[37] W. L. Liu and A. A. Balandin, J. Appl. Phys. **97**, 073710 (2005).
[38] S. Yamakawa, S. Aboud, M. Saraniti, and S. M. Goodnick, Semicond. Sci. Technol. **19**, S475 (2004).
[39] A. M. Witowski, K. Pakula, J. M. Baranowski, M. L. Sadowski, and P. Wyder, Appl. Phys. Lett. **75**, 4154 (1999).
[40] H. Wang and A. B. Chen, J. Appl. Phys. **87**, 7859 (2000).
[41] S. Dhara, A. Datta, C. T. Wu, Z. H. Lan, K. H. Chen, Y. L. Wang, Y. F. Chen, C. W. Hsu, L. C. Chen, H. M. Lin, and C. C. Chen, Appl. Phys. Lett. **84**, 3486 (2004).
[42] C. G. Van de Walle and J. Neugebauer, J. Appl. Phys. **95**, 3851 (2004).
[43] T. Mattila and R. M. Nieminen, Phys. Rev. B **55**, 9571 (1997).
[44] K. A. Bertness, N. A. Sanford, J. M. Barker, J. B. Schlager, A. Roshko, A. V. Davydov, and I. Levin, J. Electron. Mater. **35**, 576 (2006).
[45] K. A. Bertness, A. Roshko, N. A. Sanford, J. M. Barker, and A. Davydov, J. Cryst. Growth **287**, 522 (2006).
[46] W. L. Liu and A. A. Balandin, J. Appl. Phys. **97**, 123705 (2005).
[47] Data provided by Michelle Chen, University of Pennsylvania.